Sizing Optimization of Tubular Linear Induction Generator and Its Possible Application in High Acceleration Free-Piston Stirling Microcogeneration

Thu Thuy Dang, Marie Ruellan, Laurent Prevond, Hamid Ben Ahmed, Bernard Multon

Sizing Optimization of Tubular Linear Induction Generator and Its Possible Application in High Acceleration Free-Piston Stirling Microcogeneration

Thu Thuy Dang, Marie Ruellan, Laurent Prévond, Hamid Ben Ahmed, and Bernard Multon

***Abstract*—We usually find applications of rotary induction generator, direct-drive tubular linear permanent-magnet generator, etc. for the mechanoelectrical conversion process within Stirling microcogenerator systems. This paper presents the design optimization investigation for a direct-drive tubular linear induction generator for a dual free-piston Stirling microcogenerator system. On the one hand, a high oscillating frequency and a relatively long piston's travel bring about a very high acceleration of the generator's moving part, up to 1018 m/s^2. On the other hand, the tubular linear induction generator offers many interesting assets in this application: low weight mover, appearance of levitation force, no mechanical spring, low mechanical losses, no cogging force, easy manufacture, very low investment and maintenance cost, and so on. However, the tubular linear induction generator is sparsely used, because of its *a priori* relatively low energetic efficiency. This paper presents a sizing optimization approach for maximizing the performance and demonstrates that, with an astute arrangement of electrical devices, the tubular linear induction generator can constitute a well adapted solution for free-piston Stirling microcogenerator systems.**

***Index Terms*—Chain of static converters, cylindrical current sheet method, dual free-piston Stirling engine (DFPSE), experimental validation, field-oriented vector control, grid-connected, microcogeneration, model reduction, NSGA-II, optimization, traveling wave, tubular linear induction generator (TLIG).**

This work was supported by the French National Research Agency (Agence Nationale de la Recherche) under Project CETI-ANR-08-BLAN-0118.

T. T. Dang is with the G2ELab-CNRS Laboratory, 38402 Saint Martin d'Hères, France (e-mail: thu-thuy.dang@g2elab.grenoble-inp.fr).

M. Ruellan is with the SATIE-CNRS Laboratory, University of Cergy-Pontoise, 95031 Cergy-Pontoise, France (e-mail: marie.ruellan@u-cergy.fr).

L. Prévond is with the SATIE-CNRS Laboratory CNAM, 75141 Paris, France (e-mail: Laurent.prevond@cnam.fr).

H. Ben Ahmed and B. Multon are with the SATIE-CNRS Laboratory, École Normale Supérieure de Rennes, 35170 Bruz, France (e-mail: hamid.benahmed@ens-rennes.fr; Bernard.Multon@ens-rennes.fr).

NOMENCLATURE

DFPSE	Dual free-piston Stirling engine.
TLIG	Tubular linear induction generator.
μ-CHP	Microcogeneration.
FOC	Flux-oriented control.
PFC	Power factor corrector.
AC/DC	Subscripts for the three-phase converter at the generator's side.
DC/AC	Subscripts for the single-phase converter at the grid's side.
T, D	Subscripts for IGBTs and diodes.
t	time [s]
A	Vector potential [Wb/m].
ϕ	Vector potential amplitude [Wb/m].
B	Magnetic-flux density [T].
H	Magnetic field [A/m].
E	Electric field strength [V/m].
J	Current density [A/m^2].
$J_{s\theta}$	Azimuthal component of the inductor current [A/m].
J_{sm}	Magnitude of the line-current intensity [A/m].
ω_s	$= 2\pi f_s$, primary angular frequency [rad/s].
ω	Angular frequency of the network [rad/s].
ω_r	Secondary angular frequency [rad/s].
k	Wave coefficient [m^{-1}].
$\bar{P}$	Complex power [W].
P_{tr}	Power transmitted to the mover [W].
y_p	Instantaneous position of the piston/mover [m].
v_s	Exciting field velocity [m/s].
v	Piston/mover velocity [m/s].
s	slip
F_z	Axial force of the TLIM in motor mode [N].
F_{gene}	Resisting force of the TLIG in generator mode [N].
R_s	Stator (primary) resistance [Ω].
R'_r	Secondary resistance referred to the stator side [Ω].
L_m	Magnetizing inductance [mH].
L_s	Cyclic stator inductance [mH].
L_r	Cyclic mover inductance [H].
M	Stator/mover mutual inductance [mH].
l_{fs}	Stator leakage inductance [mH].
l'_{fr}	Mover leakage inductance referred to the stator side [mH].
l'_{ft}	Totalized leakage inductance [mH].
ς	Blondel coefficient.
$\bar{I}_s$	Complex stator phase current [A].
$\bar{I}_\mu$	Complex magnetizing current [A].

$\bar{I}'_r$	Complex secondary current referred to the stator side [A].
v_a,v_b,v_c	Three-phase voltage of the TLIG [V].
i_a, i_b, i_c	Three-phase generated current of the TLIG [A].
Ψ	Magnetic flux [Wb].
θ_s	Instantaneous angular position of the stator flux [rad].
ψ	Transformation angle [rad].
v_{grid}	Instantaneous grid voltage at the connecting node [V].
i_{grid}	Injected current into the grid [A].
V_{out}	Output voltage of the DC/AC converter [V].
$\langle P \rangle$	Average power [W].
P_{mec}	Instantaneous mechanical power of the DFPSE [W].
P_{gene}	Instantaneous electric power generated by the TLIG [W].
P_{grid}	Instantaneous electric power injected into the grid [W].
p_{Js}	Joule losses of the stator [W].
p_{Jr}	Joule losses of the mover [W].
$p_{\text{AC/DC}}$	Semiconductor losses of the AC/DC converter [W].
$p_{\text{DC/AC}}$	Semiconductor losses of the DC/AC converter [W].
$p_{\text{cond } T3}$	Conduction losses of the AC/DC converter's IGBTs [W].
$p_{\text{cond } D3}$	Conduction losses of the AC/DC converter's diodes [W].
$p_{\text{com } T3}$	Switching losses of the AC/DC converter's IGBTs [W].
p_{DC}	Joule losses of the DC bus capacitor [W].
S	Apparent power [VA].
α	PWM pulses.
C_{bus}	DC bus capacitor [F].
L	Inductance of the LP filter's inductor [mH].
R_L	Resistance of the LP filter's inductor [Ω].
η	Overall electric efficiency of the grid connected TLIG [%].
f_{Obj1}	Objective function 1 [W].
f_{Obj2}	Objective function 2 [€].
$\mathbf{C}$	Cost of raw material [€/kg].
$\mathbf{V}$	Volume of raw material [m^3].
I_{rated}	Rated current of static converters [A].
ρ	Density of raw material [kg/m^3].
σ	Conductivity [S/m].
μ	Permeability [H/m].
s, r	Subscripts for the stator, mover.
d, q	Subscripts for the d, q-axis of the Park reference frame.
r, θ, z	Subscripts for cylindrical coordinates.
$\Re()$, $\Im()$	Real imaginary part of quantity in brackets.
$*$	Index for setpoints.

I. Introduction

THE tubular linear induction machine (TLIM) is more often operated as a motor than as a generator. In fact, as a direct-drive linear motor, its high velocity, high force to moving mass ratio, and its possibilities to be accurately controlled make it attractive to use as industrial or social robots, machine tools, fast manipulators [1] and as high efficiency molten metal pumps [2] or rapid launchers [3], [4].

TABLE I
Advantages/Inconveniences Analysis Between Rotary and Direct-Drive Linear Generator for Microcogenerator

	Advantages	Inconveniences
Rotary generator	• Mature technology • High efficiency • Robustness	• Mechanical transmission required: bearing, crank shaft system, need for lubrication, etc. • Mechanical power losses and wears • Large size
Direct-drive generator	• No mechanical transmission: compactness, no need for lubrication • Little mechanical losses and wears • Reduced maintenance	• Including research cost for electric generator

However, the tubular linear induction generator (TLIG) exists but is seldom investigated. In this paper, we will demonstrate how the linear TLIG may be presented as a good choice for free-piston Stirling microcogenerator (μ-CHP) systems.

A. System Generality

Motorized by a dual free-piston Stirling engine (DFPSE), our system is designed with the aim to reduce noise, greenhouse gas emission, as well as to increase the traditional Stirling cycle performance (see Fig. 1). The studied μ-CHP system is designed to provide electricity and heat for homes application (typically 1 kW for electric power and 10 kW for thermal power), using only one primary energy source such as methane, solid biomass or solar heat, etc. The μ-CHP principle allows for the economization of primary energy sources due to local production and consumption together with a very high overall efficiency (heat and electricity), usually reaching 85 up to 95%.

As shown in Fig. 1, two traditional β free-piston Stirling engines share a single piston and form a so called DFPSE. The latter transforms the thermal energy that results from the external combustion into mechanical energy in the form of an oscillating translation of the piston. In order to harvest the mechanical energy of the piston without any mechanical joints (e.g., crank shaft systems), the induction generator uses the piston of the Stirling engine directly as its secondary mover (see Fig. 1 and Table I). The DFPSE and the TLIG thus share one component, the piston/mover. The DFPSE can reach very high oscillating frequencies, between 20 and 35 Hz. One can find more details about the function of the DFPSE in [5].

B. Advantages and Weaknesses of the TLIG in This Application

By reason of enhancement of the system's compactness, robustness and efficiency, the stator winding (primary) is arranged inside the piston which is sealed (see Fig. 1).

The structure does not contain mechanical springs because the closed working gas (helium) within the piston/mover reacts like a gas spring [5].

Furthermore, in a tubular linear induction machine, we know that the interaction between the magnetic traveling wave

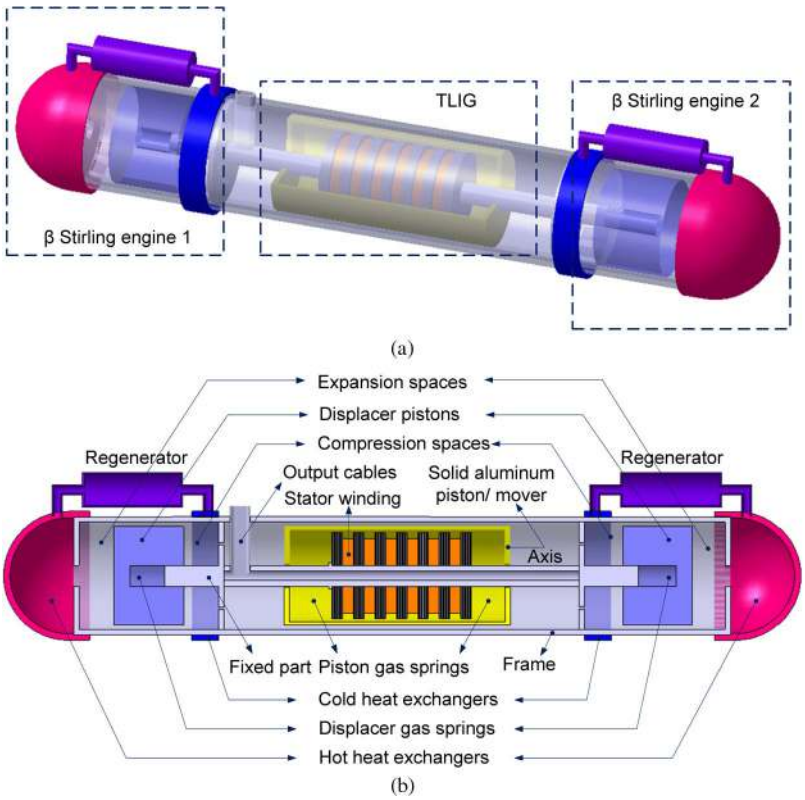

Fig. 1. (a) Structure of the μ-CHP system that uses a DFPSE and a TLIG. (b) Longitudinal cut and details of the system.

and the induced azimuthal currents generate not only axial force, but also radial force. The radial force centers (levitates) the mover during transit eliminating the need for mechanical bearing and limiting friction [6]. If this "natural levitation" of the piston/mover is controlled, the horizontal and vertical position of the system could be feasible without mechanical springs.

In addition, the stable operation of the DFPSE imposes the limited mass of the direct-drive piston/mover. This constraint can easily be satisfied by the TLIG with solid aluminum secondary (see Fig. 1).

Given the dynamics of the mechanical drive, the TLIG with a low weight aluminum mover more easily reaches high acceleration compared with the tubular linear permanent-magnet generator (TLPMG). which contains a high weight magnet mover.

The main drawback of the TLIG structure is its energetic performance which is often known to be low. This is due not only to necessary secondary Joules losses but also to a large air-gap [7], [8].

However, the arrangement of the TLIG inside the two β Stirling engines (see Fig. 1) allows the TLIG to be in contact with the gas of the compression spaces which is water-cooled at a temperature of 40 °C –90 °C. In other words, the whole electric generator (stator and mover) is immersed in the working gas of the two cool spaces, the flow of the gas allows for its forced cooling (see Fig. 1). Therefore, heat from the Joule losses and iron losses can be harvested for the thermal load.

Above all, the TLIG structure offers a very low investment and operating cost with little need for maintenance since there are only three moving parts: two displacers and the piston/mover. The economic criteria becomes extremely important in home application.

TABLE II
ADVANTAGES/INCONVENIENCES ANALYSIS OF TLIG AND TLPMG IN STIRLING MICROCOGENERATOR SYSTEM

	Strong suits	Weaknesses
Direct-drive TLIG	• Very high acceleration: low weight mover, levitation force • Simple mechanism: no springs, zero mechanical wears, little maintenance, very low mechanical power losses • Compactness • Zero cogging torque • Low cost	• A priori low efficiency ○ Secondary Joules losses ○ Large air-gap ➔ But in this application, Joules and iron losses can be harvested for thermal load.
Direct-drive TLPMG	• High efficiency: low losses • High acceleration but springs required	• Springs required: heavy weight mover, no levitation force, mechanical losses and wears due to springs • Cogging force • High cost due mainly to the use of rare earth

In direct-drive generator technology, the TLPMG presents a high-performance and is largely researched. However, with a heavy mover, the TLPMG is usually exploited at limited acceleration such as sea wave's energy harvesting system [9]–[11]. In the hybrid electric vehicle domain, the acceleration of permanent-magnet motor/generator can attain

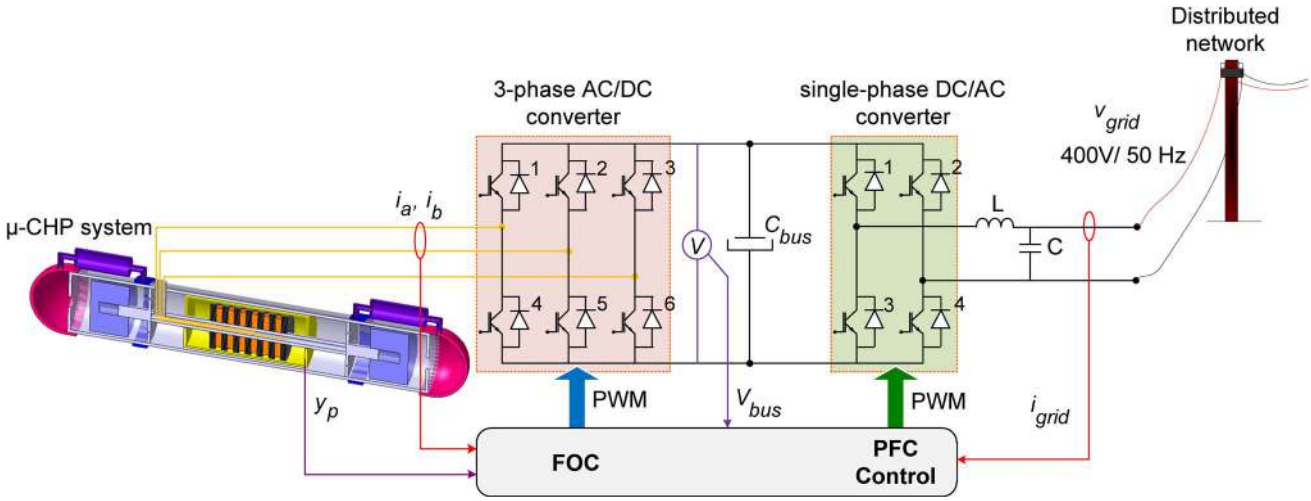

Fig. 2. Complete TLIG-to-grid configuration in this optimization framework.

up to 300–400 m/s^2 [12], [13]. However, a heavy weight moving magnet usually requires mechanical springs with enough stiffness to hold the moving part in position. The higher the dynamic is, the more important mechanical losses and wears there are.

C. Objective and Outline

The motivation concerns the design of the TLIG. The aim is to improve its energetic efficiency in order to fully benefit from its advantages (see Table II).

The following questions will be answered: 1) what is the highest performance that can be achieved by the TLIG in this application? 2) for the conception phase of the DFPSE, what are influences of the operating point of free-piston Stirling engine on the performance of the TLIG?

In this paper, a complete TLIG-to-grid configuration is considered. The research of the optimal overall performance will also include the static converters' efficiency (see Fig. 2).

First, a pseudoanalytical model in motor mode using the current sheet method and considering a multilayer cross section of the tubular structure, is developed. Poynting vectors are calculated in order to compute the axial thrust force and the equivalent circuit's lump parameters. This model is then experimentally validated (see Section II-B).

A complete simulation of the entire grid-connected microcogenerator system is implemented using MATLAB/Simulink. The simulation contains multiphysic models with control loops which help to examine the transient behavior of subsystems (DFPSE, TLIG, and AC/DC/AC converters) and to calculate the overall electric efficiency (see Section II-C).

Next, because of the important runtime of the aforementioned simulation, a model reduction of the system has been built in order to quickly obtain the overall electric efficiency (see Section III-A).

After, the optimization process which implements the pseudoanalytical model, the reduced model of the grid-connected system and the genetic algorithm NSGA-II, provides interesting results about the performance of the TLIG in this application (see Section III-C). The magnetizing current component is one of the parameters taken into account. The active power injected into the grid and the total cost are two criteria, which decide the optimal configurations.

Lastly, the influence of the Stirling engine's operating point on the performance of the TLIG is discussed (see Section III-C3).

II. Modeling and Simulation of the Entire System

A. Analysis of the TLIG

1) Pseudoanalytical Model: The electromagnetic model of the TLIG using the cylindrical current sheet method presented in [14] and [15], allows for the prediction of the axial force (in motor mode) versus supply frequency and the equivalent circuit's lump parameters. The structure of the TLIG is shown in Fig. 3(a). The cylindrical coordinates are used.

The simplifying assumptions adopted are as follows.

1) The magnetic circuit is nonsaturable.
2) The flux density is sinusoidal in the air-gap along the z-axis.
3) The flux density magnitude is considered as invariant along the z-axis as a cross section of the machine showing the five concentric layers is sufficient to understand the electromagnetic field in the machine [Fig. 3(b)].
4) The conductivity of the iron core is supposed to be negligible so as there is no eddy-current in the iron core.

The infinite length current sheet is placed at the radii of the stator winding (Fig. 3). However, in order to take into account the finited length of the stator winding, a Fourier series development of the inductor current in time and in space, along the z-axis, is used (see Appendix).

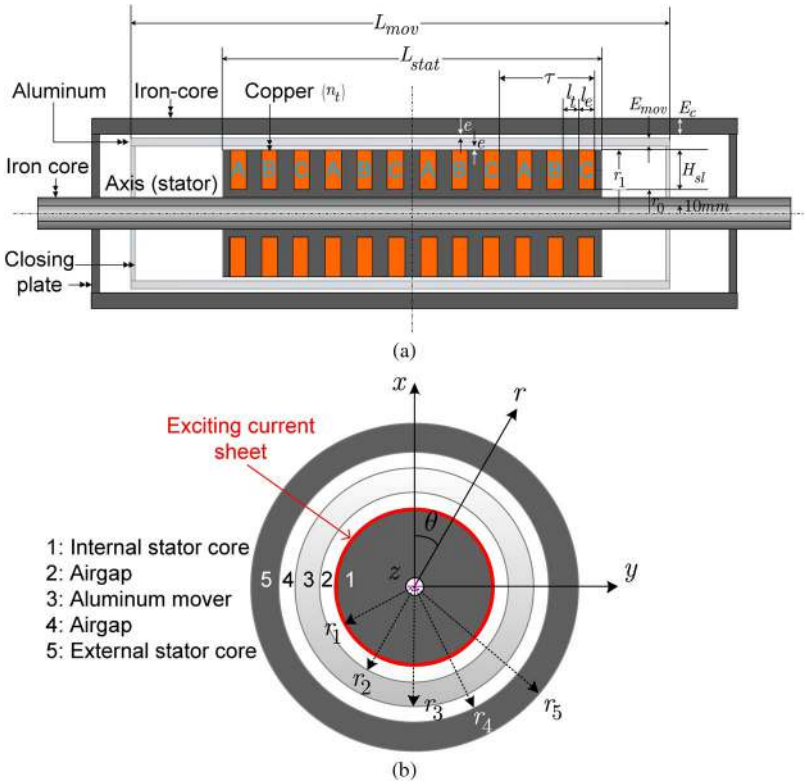

Fig. 3. (a) Longitudinal section. (b) Multilayer transverse section of the studied TLIG.

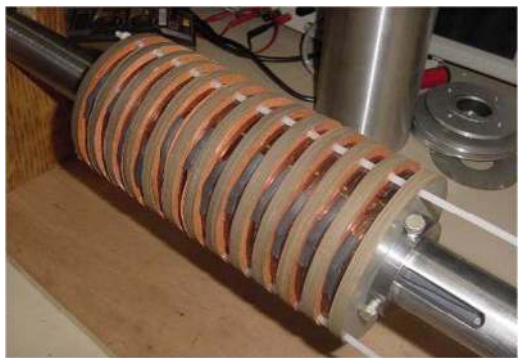

Fig. 4. 1-kW TLIM prototype: Internal stator winding.

Neglecting the displacement current, Maxwell's equations written for every point in the machine are

$$\vec{\nabla} \times \vec{B} = \mu \vec{J} \tag{1}$$

$$\vec{\nabla} \times \vec{E} = -\frac{\partial \vec{B}}{\partial t} \tag{2}$$

$$\vec{J} = \sigma(\vec{E} + \vec{v} \times \vec{B}) \tag{3}$$

$$\vec{\nabla} \times \vec{A} = \vec{B}. \tag{4}$$

The inductor current thus only has one component along the azimuthal axis (θ), it is modeled by a wave equation along the longitudinal z-axis

$$J_{s\theta} = J_{sm} e^{j(\omega_s t - kz)}. \tag{5}$$

Where

- $J_{sm} = \sqrt{2} n_t I_s / l_e$ magnitude of the line-current intensity [A/m];
- $k = \pi/\tau$ wave coefficient.

Therefore, one can demonstrate that the potential vector $\vec{A}$ also only has one nonzero component along the θ-axis

$$\vec{A} = A_\theta \overrightarrow{u_\theta} = \phi(r) e^{j(\omega_s t - kz)} \overrightarrow{u_\theta}. \tag{6}$$

From (1), (3), and (4), we can obtain

$$\vec{\nabla} \times \vec{\nabla} \times \vec{A} = \mu\sigma \left(-\frac{\partial \vec{A}}{\partial t} - v \frac{\partial A_\theta}{\partial z} \overrightarrow{u_\theta} \right). \tag{7}$$

Taking only the θ-component from both sides of (7), and after rearranging, we have

$$\frac{\partial^2 \phi}{\partial r^2} + \frac{1}{r} \frac{\partial \phi}{\partial r} - \left(\frac{1}{r^2} + \gamma^2 \right) \phi = 0 \tag{8}$$

where we define $\gamma^2 = k^2 - j s \omega_s \mu \sigma$.

Equation (8) has solutions as modified Bessel functions of the first and second kind with the new variable $u = \gamma r$. The

expression of the vector potential for each layer can be written as the following:

$$\vec{A} = [CI_1(\gamma r) + DK_1(\gamma r)]\, e^{j(\omega_s t - kz)} \vec{u}_\theta. \quad (9)$$

From (2), (4), and (9), the expressions of the orthoradial electric field and the axial magnetic field can also be derived

$$\vec{E}_\theta = j\omega_s\, [CI_1(\gamma r) + DK_1(\gamma r)]\, e^{j(\omega_s t - kz)} \vec{u}_\theta \quad (10)$$

$$\vec{H}_z = \frac{\gamma}{\mu}\, [CI_0(\gamma r) + DK_0(\gamma r)]\, e^{j(\omega_s t - kz)} \vec{u}_z. \quad (11)$$

Where C and D are constants to be determined for the n-layer (1 to 5) from boundary condition [15]. To reflect the effective air-gap extension due to open slots, the Carter factor is introduced into the model, Appendix.

2) Power Calculation: In sinusoidal mode, the complex power carried by the electromagnetic field through a tubular surface of 1-m length is given as

$$\bar{P} = \frac{1}{2} E_\theta(\gamma r) H_z^*(\gamma r)(2\pi r)\ \text{[W/m]}. \quad (12)$$

Thus, the complex power transmitted to the mover is the difference between the incoming and outgoing power of its volume (layer 3, Fig. 3)

$$\overline{P_{tr}} = \bar{P}(r_2) - \bar{P}(r_3). \quad (13)$$

3) Developed Axial Force: The axial force (in motor mode) can be calculated as

$$F_z = \frac{\Re(\overline{P_{tr}})}{v_s}\text{[N]} \quad (14)$$

with $v_s = \omega_s/k$ the exciting field velocity [m/s].

4) Consideration of Slots and Ends Effects: The development of the traveling wave inductor current in the Fourier series allows for the correction of this method to take into account the slots and ends effects [16], [17]. In our case, the expression of the inductor current's spatial distribution is presented in Appendix.

B. Experimental Validations of the Pseudoanalytical Model & Field-Oriented Vector Control

1) Experimental Prototype: On the one hand, the cylindrical current sheet hypothesis is an approach which allows for an analysis of the electromagnetic phenomena of TLIMs. With the purpose of validating the pseudoanalytical model using current sheet method, a 1-kW (electric) TLIM prototype has been built, Figs. 4 and 5.

On the other hand, the disposition of the prototype is also valuable for testing its appropriate control strategy.

The magnetic circuit was made with sheets of FeSi, type M330. The geometric and electric data (presented in Fig. 3), are specified in Table III.

2) Validation of the Force Characteristic: As shown in Fig. 6, the measurements are taken with a constant stator current (Table III) and with a variable supply frequency from 10 to 50 Hz under stand-still conditions. The theoretical results

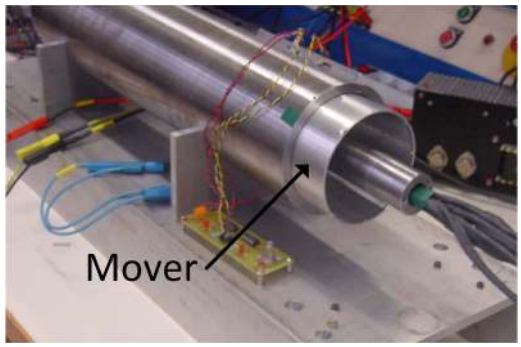

Fig. 5. 1-kW TLIM prototype: Solid aluminum mover, axis with output cables, and outer stator iron core.

TABLE III
EXPERIMENTAL TLIM'S DATA

Stator winding radius [mm]	r_1	54
Internal stator winding radius [mm]	r_0	22
Actual air-gap thickness [mm]	e	0.5
Aluminum mover thickness [mm]	E_{mov}	2
Outer stator iron-core thickness [mm]	E_c	10
Number of phases	m	3
Poles	$2p$	4
Slot per pole per phase	--	1
Coil width [mm]	l_e	8
Slot pitch [mm]	$l_e + l_t$	16
Height slot [mm]	H_{sl}	32
Pole pitch [mm]	τ	48
Stator length [mm]	L_{stat}	192
Mover's length [mm]	L_{mov}	400
Turns per slot	n_t	44
Conductor cross-section [mm^2]	S	4
Average length of a turn [mm]	--	217
Copper filling factor	k_{coil}	0.95
Copper conductivity [S/m]	σ_{Cu}	59.10^6
Mover conductivity [S/m]	σ_{Alu}	36.10^6
Vacuum permeability [H^{-1}]	μ_0	$4\pi.10^{-7}$
Relative permeability of the iron core	μ_{Fe}	5000
R.M.S stator phase current [A]	I_s	10
Frequency [Hz]	f_s	50

are obtained in the same condition, meaning that $s = 1$. The experimental measurements of the axial force are very close to the theoretical results, with a mean deviation of 4.5%. Thus, this shows the first validation of the pseudoanalytical model.

3) Validation of Equivalent Circuit's Lump Parameters: The prototype is also used to validate the calculation of the equivalent circuit. The experimental tests have allowed for the identification of the circuit's elements in Fig. 7.

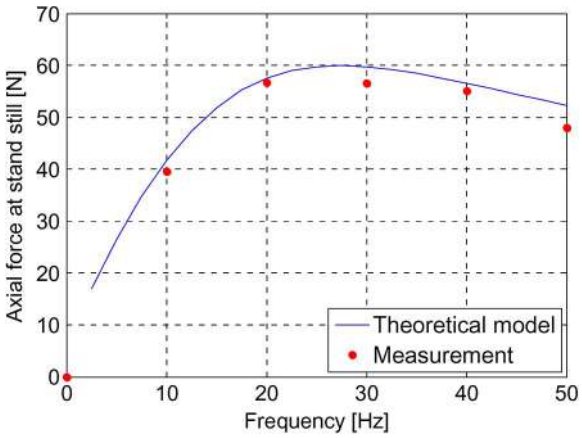

Fig. 6. Experimental validation of the axial force characteristic versus supply frequency at standstill.

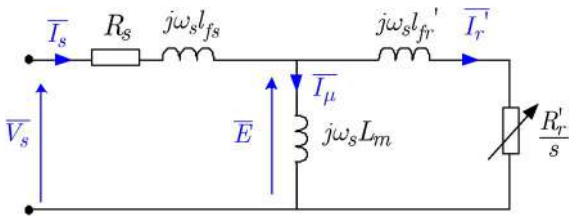

Fig. 7. Per-phase equivalent circuit used in the measurements.

On the one hand, to identify L_s, the aluminum secondary is removed (test without mover). So, the inductor current must be low (< 1.0 A) as not to saturate the magnetic circuit.

On the other hand, to determine the " nonaccessible" parameters relative to the mover (l'_{fr} and R'_r), the machine is tested under stand-still conditions (locked mover, $s = 1$) and the inductor current is 10 A R.M.S (50 Hz).

The stator resistance R_s is measured by means of a DC test.

While determining these parameters from the pseudoanalytical model, note that the latter is not capable of evaluating the stator resistance and the stator leakage inductance. These parameters have to be calculated independently (see Appendix). However, it enables the calculation of the magnetizing inductance and secondary parameters.

First, the magnetizing inductance can be obtained with the knowledge of the power transiting through the tubular surface of the current sheet, whereas the third zone [Fig. 3(b)] is treated as air ($\mu_r = 1$ and $\sigma = 0$) in order to simulate the removed mover. We deduce

$$L_m = M = \frac{\Im\left[\overline{P}(r_1)\right]}{3\omega_s I_s^2}. \tag{15}$$

The stator current may be selected as the reference phasor. Knowing M, we can find L_s by adding the stator leakage inductance (see Appendix).

Additionally, at standstill, the secondary frequency is equal to the primary frequency. Then, $1'_{fr}$ and R'_r can be determined

TABLE IV
EQUIVALENT CIRCUIT'S LUMP PARAMETERS

Parameters	R_s	L_s	l_{ft}'	R_r'
Measurements	0.3 Ω	10 mH	5.0 mH	3.4 Ω
Theoretical results	0.3 Ω	11 mH	5.2 mH	3.7 Ω

from the power transmitted to the mover

$$l'_{fr} = \frac{\Im\left[\overline{P}(r_1)\right] - 3j\omega_s L_m |\overline{I}_\mu|^2}{3j\omega_s \left|\overline{I}'_r\right|^2} \tag{16}$$

$$R'_r = \frac{\Re\left[\overline{P}(r_1)\right]}{3\left|\overline{I}'_r\right|^2} = \frac{\Re[\overline{P_{tr}}]}{3\left|\overline{I}'_r\right|^2} \tag{17}$$

where $|\overline{I}_\mu|$ and $|\overline{I}'_r|$ are, respectively the magnitudes of the complex magnetizing and secondary currents. They can be easily found by knowing $\overline{P}(r_1)$ and I_s.

The Table IV shows the appreciable agreement between the measurements and the pseudoanalytical model's results for the equivalent circuit's lump parameters.

Indeed, the lump parameters shown in Table IV take into account the slots and end effects. They can be used in order to establish the dynamic model in the Park reference frame which takes into account the transient behavior of the generator for vector control.

4) Implementation of Flux-Oriented Vector Control: The rotor flux-oriented vector control (FOC) which uses fixed parameters (Table IV) has been achieved experimentally. Its detail is presented in Fig. 9(b).

The vector control has provided the axial force (noted F_z because of the motor mode) which perfectly follows its sinusoidal setpoint at high mechanical frequency, 50 Hz [Fig. 8(a)]. In practice, the I_{sq} component of the stator current is regulated but not the axial force. However, if the rotor flux is controlled to remain constant, the I_{sq} component is directly proportional to the axial force

$$F_z = \left(\frac{3\pi M}{2\tau L_r}\Psi_{rd}\right) I_{sq}. \tag{18}$$

Knowing the equivalent circuit's lump parameters, we can calculate the proportion between F_z and I_{sq}. Here, we have found a ratio of 6 between these two magnitudes [Fig. 8(a)].

This implementation of the rotor flux-oriented vector control (FOC) using fixed parameters proves that this control can successfully manage the resisting force of the TLIG once integrated into the whole system, proving, once again, the accuracy and the validity of the equivalent circuit's lump parameters determined in Table IV.

The validated pseudoanalytical model which allows for the prediction of the equivalent circuit's lump parameters from geometric data of the TLIG, can be exploited in an optimization process. In Fig. 10, a synoptic of the TLIG's pseudoanalytical model is presented.

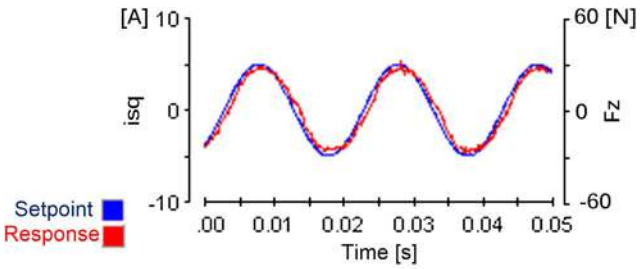

(a)

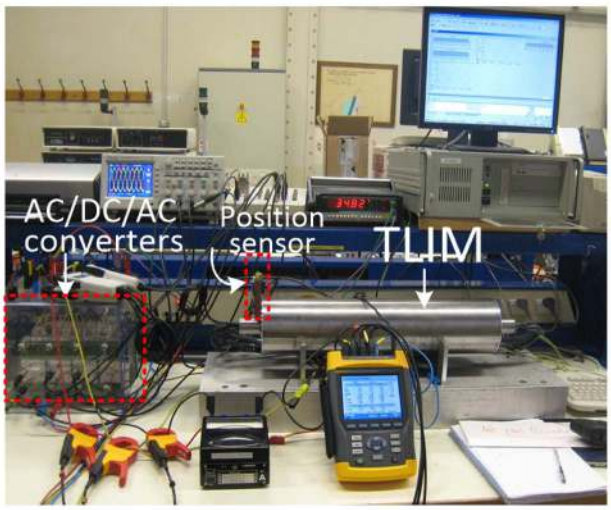

(b)

Fig. 8. (a) Experimental result of the force control for the TLIM. (b) Test bed for the vector control.

C. Complete Simulation of the μ-CHP System

1) Aspects: We now consider the operation of the TLIG in generator mode, driven by the DFPSE. The TLIG of the μ-CHP system is connected to the grid through a chain of static converters, Fig. 2. From now on, the axial force developed by the TLIG is noted F_{gene}.

A simulation of the μ-CHP system has been achieved using MATLAB/Simulink, taking into account the following aspects:

1) the multiphysic coupled models of the DFPSE + TLIG + AC/DC/AC static converters + infinite grid;
2) the time-profile of all system's physical magnitudes;
3) the effectiveness of control loops;
4) the overall electrical efficiency of the grid-connected TLIG.

As shown in Fig. 9(b), from the left to the right, the block diagrams correspond to each subsystem of the μ-CHP system: the DFPSE, the TLIG, the AC/DC converter, the DC bus capacitor, the DC/AC converter and the grid. Block diagrams of physical devices are located on the upper side, whereas the control loops are on the lower side.

2) Modeling, Control and Function of the DFPSE: Among three moving parts within the DFPSE (the two displacers and the piston/mover, Fig. 1), only the piston/mover displacement is controlled by means of the FOC (electromagnetic force feedback loop) and the P.I.D. controller (position feedback loop), Fig. 9(b).

The analytical thermodynamic model of the DPFSE (more details in [5]) allows for the prediction of the stable displacement of the piston and the two displacers from the functional and geometric data such as temperature of the hot (T_c) and cold (T_f) spaces (Fig. 9), mass, initial volumes and pressures, and so on (not shown in Fig. 9).

Displacement of the piston/mover is supposed to have a sinusoidal waveform. For a good efficiency and for the stability of the DFPSE, the resisting force F_{gene} of the TLIG should be managed in such a way that its action should be similar to a damper toward the DFPSE, (19). This means that the piston's velocity is imposed by the DFPSE, whereas the TLIG responds to the DFPSE's drive by imposing a resisting force [Fig. 9(b)]

$$F_{\text{gene}} = -C_p v \tag{19}$$

where C_p [Nm^{-1}s] is the viscous damping coefficient that must be calculated in order to obtain the desired ouput mechanical power delivered by the Stirling engine

$$C_p = \frac{\langle P_{\text{mec}} \rangle}{2\pi^2 f_{\text{osc}}^2 y_{p\_\max}^2}. \tag{20}$$

The operating point of the DFPSE is characterized by a combination of the piston stroke's amplitude and the resonant oscillating frequency $(y_{p\_\max}, f_{\text{osc}})$, or a combination of the temperature of hot and cold spaces (T_c, T_f). This study is based on only one operating point where the system is expected to work for most of the time. System data is specified in Table V and is also used in the optimization problem.

3) Modeling, Control and Function of the TLIG: As a traditional rotary induction generator, a dynamic model in the Park reference frame can be developed for the TLIG. This dynamic model uses constant lump parameters taking into account the ends effect of the linear structure (Table IV).

In this simulation, a P.I.D. controller is used in the external feedback loop in order to ensure the piston's position control. Thus, the setpoint of the resisting force $([F^*_{\text{gene}}])$ is obtained from the P.I.D controller [Fig. 9(b)]. To acquire the instantaneous resisting force, the flux-oriented vector control (FOC) is used (Section II-B4). In this application, the TLIG is never in a steady state. In other words, the electric transient mode is endless so the currents generated are not sinusoidal. In fact, they even present an important offset value which can greatly amplify the Joule losses and the semiconductor losses.

4) Modeling, Control, and Function of Static Converters: Before injecting the TLIG's power into the network, the chain of static converters aids in transforming the currents' waveform into sinusoidal waveform which is in phase with the grid voltage at connection node (400 V, 50 Hz). The chain is composed of a three-phase AC/DC converter, a DC bus capacitor, a single-phase DC/AC converter and a low-pass LC filter. In this simulation, models with functional approach (not structural approach) of static converters are provided.

In Fig. 9, the Power Factor Corrector (PFC) control is applied to the single-phase converter DC/AC to ensure the sinusoidal waveform of the injected current into the grid and to maintain

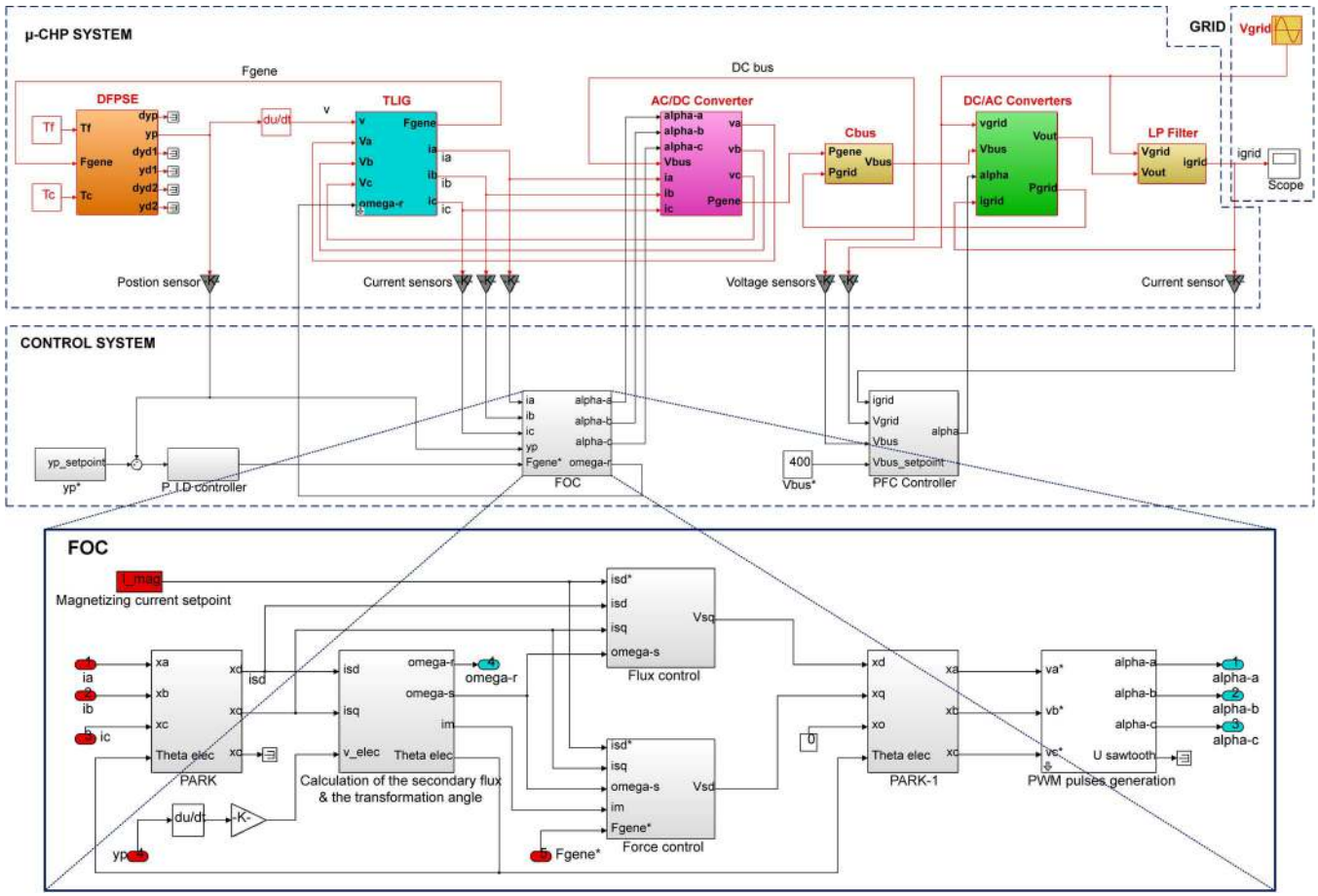

Fig. 9. Complete simulation of the grid-connected μ-CHP system using DFPSE and TLIG.

TABLE V
SYSTEM DATA FOR OPTIMIZATION EXAMPLE

Hot space temperature [K]	T_c	650
Cold space temperature [K]	T_f	320
Amplitude of the piston's stroke [cm]	$y_{p\ \max}$	2.23
Oscillation frequency [Hz]	f_{osc}	27.7
Piston's mechanical cycle [s]	T_{osc}	0.036
Viscous friction coefficient [Nm^{-1}s]	C_p	167.1
Maximum force [N]	$\max\left(F_{gene}\right)$	648
Maximum velocity [m/s]	$\max\left(v\right)$	3.9
Maximum acceleration [m/s^2]	$\max\left(\dot{v}\right)$	675
Average mechanical power [W]	$\left\langle P_{mec}\right\rangle$	1260
DC bus voltage [V]	V_{bus}	400
Power electronic switching frequency [Hz]	f_{sw}	10000

the DC bus voltage constant at 400 V (with maximum ripple of $\pm$ 5%).The overall electrical efficiency is given by

$$\eta = \frac{\langle P_{\text{grid}}\rangle}{\langle P_{\text{mec}}\rangle} = \int_{T_{\text{start}}}^{T_{\text{stop}}} i_{\text{grid}} v_{\text{grid}} dt \Big/ \int_{T_{\text{start}}}^{T_{\text{stop}}} v F_{\text{gene}} dt. \quad (21)$$

Where T_{start} is the instant of the beginning of the oscillating steady state and T_{stop} is the end of the simulation which is superior to the piston's mechanical cycle (Table V).

In conclusion, the complete simulation was first built with the aim to provide understanding about transient behavior and performance of the μ-CHP system. However, because of its very important runtime (10 min), the complete simulation is not adapted to be used in the iterative optimization process. We thus have to reduce the complete simulation in order to more quickly compute the overall electrical efficiency.

III. SIZING OPTIMIZATION OF THE GRID-CONNECTED TLIG

A. Model Reduction

1) Simplifying Assumptions: In order to obtain a model reduction and to quickly calculate the overall electric efficiency of the grid-connected TLIG, the following simplifying assumptions are proposed:

1) oscillating steady state with fixed operating point, Table V.
2) weak coupling between the DFPSE and the TLIG.
3) perfect regulation of all control loops.
4) PWM pulses considered to be continuous functions of which instantaneous values are floating mean values of PWM pulses within each switching period $(1/f_{sw})$.

5. modeling for one mechanical cycle (piston/mover's round-trip $(0, T_{\rm osc})$ with $T_{\rm osc} = (1/f_{\rm osc})$ (Table V).

2) Reduced Model: The interaction of the DFPSE and the TLIG is characterized by two physical quantities: the piston's velocity $v = \dot{y}_p$ and the resisting electromagnetic force $F_{\rm gene}$ In case of a weak coupling between the DFPSE and the TLIG, these two magnitudes are always sinusoïdal and $F_{\rm gene}$is in opposite phase with $v = \dot{y}_p$ And if the P.I.D. control and the FOC are supposed to be perfect, these magnitudes are superimposed on their setpoints

$$v = \dot{y}_p = \dot{y}_p^* = -2\pi f_{\rm osc} y_{p\_\max} \sin\left(2\pi f_{\rm osc} t\right) \quad (22)$$

$$F_{\rm gene} = F_{\rm gene}^* = 2\pi C_p f_{\rm osc} y_{p\_\max} \sin\left(2\pi f_{\rm osc} t\right). \quad (23)$$

By knowing the electromagnetic force and the velocity of the piston/mover, we derive the voltage and currents generated by the TLIG due to the lump parameters of the equivalent circuit.

First, in the hypothesis where the FOC is perfect, the d-axis secondary flux is equal to its constant setpoint

$$\Psi_{rd} = \Psi_{rd}^*. \quad (24)$$

Consequently, the two components of the stator current in the Park reference frame can be found by

$$I_{sd} = \frac{\Psi_{rd}}{M}\sqrt{\left(\frac{L_r}{R_r}\right)^2 + 1} \quad (25)$$

$$I_{sq} = \frac{2}{3}\frac{\tau L_r}{\pi M \Psi_{rd}} F_{\rm gene}. \quad (26)$$

The transformation angle is equal to the angular position of the stator flux in the fixed coordinate system

$$\psi = \theta_s = \int_0^{T_{\rm osc}} \omega_s dt = \frac{\pi}{\tau} - \frac{2}{3} C_p \frac{\tau R_r}{\pi \Psi_{rd}^2}\left(y_p - y_{p\_\max}\right). \quad (27)$$

The d and q axis stator voltages in the generator- convention are then found by

$$V_{sd} = -R_s I_{sd} + \varsigma L_s \omega_s I_{sq} \quad (28)$$

$$V_{sq} = -R_s I_{sq} - \varsigma L_s \dot{I}_{sq} - \omega_s \varsigma L_s \dot{I}_{sd} - \omega_s \frac{M}{L_r}\Psi_{rd} \quad (29)$$

hence $\varsigma = 1 - (M^2/L_s L_r)$ is the coefficient of Blondel.

The currents and voltages of three phases a, b and c can be readily found by the inverse Park transformation. After, in the hypothesis where the PFC control is perfect, the DC bus voltage is superimposed with its setpoint, 400 V

$$V_{\rm bus} = V_{\rm bus}^*. \quad (30)$$

The duty cycle of the three-phase AC/DC converter can be found by

$$\alpha_x = \frac{1}{2} + \frac{v_x}{V_{\rm bus}} \text{ with } x = a, b, c. \quad (31)$$

TABLE VI
CURRENTS OF THE THREE-PHASE AC/DC CONVERTER

	i_{T1}	i_{D1}	i_{T4}	i_{D4}
$i_a \geq 0$	$\alpha_a i_a$	0	0	$(1-\alpha_a) i_a$
$i_a < 0$	0	$\alpha_a i_a$	$(1-\alpha_a) i_a$	0
	i_{T2}	i_{D2}	i_{T5}	i_{D5}
$i_b \geq 0$	$\alpha_b i_b$	0	0	$(1-\alpha_b) i_b$
$i_b < 0$	0	$\alpha_b i_b$	$(1-\alpha_b) i_b$	0
	i_{T3}	i_{D3}	i_{T6}	i_{D6}
$i_c \geq 0$	$\alpha_c i_c$	0	0	$(1-\alpha_c) i_c$
$i_c < 0$	0	$\alpha_c i_c$	$(1-\alpha_c) i_c$	0

TABLE VII
CURRENTS OF THE SINGLE-PHASE DC/AC CONVERTER

	i_{T1}	i_{T4}	i_{T2}	i_{T3}
$i_{grid} \geq 0$	αi_{grid}	αi_{grid}	0	0
$i_{grid} < 0$	0	0	$-(1-\alpha) i_{grid}$	$-(1-\alpha) i_{grid}$
	i_{D1}	i_{D4}	i_{D2}	i_{D3}
$i_{grid} \geq 0$	0	0	$(1-\alpha) i_{grid}$	$(1-\alpha) i_{grid}$
$i_{grid} < 0$	$-\alpha i_{grid}$	$-\alpha i_{grid}$	0	0

The formula that gives the instantaneous currents passing through each semiconductor switch of the AC/DC converter are specified in Table VI where IGBTs are rated T_1 to T_6 and diodes D_1 to D_6 (Fig. 2).

The hypothesis where the PFC control is perfect also permits us to deduce the current injected into the network which must be sinusoïdal and in phase with the grid voltage

$$i_{\rm grid} = I_{\rm grid\_\max} \sin(\omega t) \quad (32)$$

where $I_{\rm grid\_\max}$ has to be determined in the next section.

The duty cycle of the DC/AC single phase converter can be found by knowing the ouput voltage of the converter

$$\alpha = \frac{1}{2} + \frac{V_{\rm out}}{2V_{\rm bus}} \quad (33)$$

hence $V_{\rm out}(t)$ is different from $V_{\rm grid}(t)$ because of a voltage drop across the inductance of the LP filter (see Fig. 9).

3) Power Balance: The instantaneous mechanical power generated by the DFPSE is written as

$$P_{\rm mec} = -F_{\rm gene}\dot{y}_p = 2\pi^2 C_p f_{\rm osc}^2 y_{p\_\max}^2 - 2\pi^2 C_p f_{\rm osc}^2 y_{p\_\max^2} \cos\left(4\pi f_{\rm osc} t\right). \quad (34)$$

The instantaneous electric power generated by the TLIG is given as the sum of

$$P_{\rm gene} = \frac{3}{2}(V_{sd} I_{sd} + V_{sq} I_{sq}). \quad (35)$$

The difference between $P_{\rm mec}$ and $P_{\rm gene}$ shows the total Joule losses because the iron losses are not taken into account in this

model, and the mechanical losses are negligible since there is no direct contact between the piston/mover and the fixed part

$$p_{Js} = \frac{3}{2}\frac{R_s}{T_{\rm osc}}\int_0^{T_{\rm osc}} \sqrt{I_{sd}^2 + I_{sq}^2}dt \tag{36}$$

$$p_{Jr} = \frac{3}{2}\frac{R_r}{T_{\rm osc}}\int_0^{T_{\rm osc}} \sqrt{I_{rd}^2 + I_{rq}^2}dt. \tag{37}$$

The static converters losses must be taken into account to derive the electrical power sent to the network. Two types of semiconductor losses are considered: conduction losses and switching losses. For the three-phase AC/DC converter, conduction losses are calculated by

$$p_{\rm cond\_T3} = \sum_{i=1\div 6}\frac{1}{T_{\rm osc}}\left(V_{CE0}\int_0^{T_{\rm osc}} i_{Ti}dt + R_{CE0}\int_0^{T_{\rm osc}} i_{Ti}^2 dt\right) \tag{38}$$

$$p_{\rm cond\_D3} = \sum_{i=1\div 6}\frac{1}{T_{\rm osc}}\left(V_{D0}\int_0^{T_{\rm osc}} i_{Di}dt + R_{D0}\int_0^{T_{\rm osc}} i_{Di}^2 dt\right) \tag{39}$$

and switching losses are calculated by

$$p_{\rm com\_T3} = \frac{2f_{sw}V_{\rm bus}}{V_{\rm test}} \times \left[(b_{\rm on}+b_{\rm off})\sum_{1\div 6}\int_0^{T_{\rm osc}}(i_{Ti}+i_{Di})\,dt + \frac{a_{\rm on}+a_{\rm off}}{2}\right]. \tag{40}$$

- $V_{\rm CE0}$, $R_{\rm CE0}$, V_{D0}, R_{D0} are data of IGBTs and diodes, extracted from datasheet (see the Appendix).
- $a_{\rm on}$, $a_{\rm off}$, $b_{\rm on}$, $b_{\rm off}$ are coefficients of a linear model of dissipated energy achieved by tests under the voltage $V_{\rm test}$ (see the Appendix).

Then, three-phase AC/DC converter losses are the sum of

$$p_{\rm AC/DC} = p_{\rm cond\_T3} + p_{\rm cond\_D3} + p_{\rm com\_T3}. \tag{41}$$

The losses of the DC/AC converter can be calculated in the same way, in the condition in which the waveform of $i_{\rm grid}$ is known (Table VII). However, we cannot determine $i_{\rm grid}$, particularly $I_{\rm grid\_max}$, if we do not know $P_{\rm grid}$. In addition, like a snake biting its own tail, $P_{\rm grid}$ cannot be deduced without the result of the DC/AC converter's losses.

However, we can remark that the DC/AC converter's losses and the DC bus capacitor's losses are very little compared with the losses of the AC/DC converter. Then we can determine $I_{\rm grid\_max}$ by

$$I_{\rm grid\_max} = \frac{2(\langle P_{\rm gene}\rangle - p_{\rm AC/DC})}{V_{\rm grid\_max}}. \tag{42}$$

We obtained the instantaneous power sent into the grid once was extracted the sum of losses. Joule losses of the DC capacitor are also present in the expression of the overall electrical efficiency of the grid-connected TLIG

$$\eta = \frac{P_{\rm mec} - p_{Js} - p_{Jr} - p_{\rm AC/DC} - p_{\rm DC/AC} - p_{\rm DC}}{P_{\rm mec}}. \tag{43}$$

To conclude this paragraph, the calculation of the overall electric efficiency in oscillating steady state by the "reduced model" is thus adapted to the optimization process because it only lasts 50 ms. The synoptic of the "reduced model" is shown in the Fig. 10.

B. Optimization Problem Description

1) Multi-Objective:

a) Maximize the average electric power to the grid: The objective is to maximize the overall electrical efficiency and can be expressed by

$$f_{\rm Obj1} = \frac{1}{T_{\rm osc}}\int_0^{T_{\rm osc}} P_{\rm grid}\,(t)\,dt. \tag{44}$$

b) Minimize the total cost of "TLIG + power converters": The cost of the TLIG is the sum of the cost of the raw materials (copper, iron and aluminum), Table VIII

$$\mathbf{C}_{\rm TLIG} = \mathbf{C}_{\rm Al}\rho_{\rm Al}\mathbf{V}_{\rm mov} + \mathbf{C}_{\rm Cu}\rho_{\rm Cu}\mathbf{V}_{\rm coil} + \mathbf{C}_{\rm Fe}\rho_{\rm Fe}\mathbf{V}_{\rm core}. \tag{45}$$

The cost of converters generally depends on the number of switches, the rated current and the DC rated voltage, etc. Based on data relating to available products on the market in 2012, an empirical formula of converters' cost is given as (see the Appendix)

$$\mathbf{C}_{\rm AC/DC\ or\ DC/AC} = 1.09N(I_{\rm rated}V_{\rm bus})^{0.46}. \tag{46}$$

- $\mathbf{C}$, ρ are the cost of the raw materials [/kg] and the density for the raw materials [kg/m^3].
- $\mathbf{V}$ as the volume of the raw materials [m^3].
- $N = 3$ for the AC/DC converter and for $N = 2$ DC/AC converter.
- $I_{\rm rated}$ is the converters' rated current [A].

The second objective function can be given as

$$f_{\rm Obj2} = \mathbf{C}_{\rm TLIG} + \mathbf{C}_{\rm AC/DC} + \mathbf{C}_{\rm DC/AC}. \tag{47}$$

2) Multi-Variable: Ten Variables Should be Optimized.

a) Concerning the TLIG: There are seven geometric parameters: r_0, H_{sl}, $E_{\rm mov}$, τ, p, E_c, n_t, [see Fig. 3(a), Table III], and the magnetizing current

b) Concerning the static converters: There are two rated currents noted by $I_{\rm rated\_\ AC/DC}$,$I_{\rm rated\_\ DC/AC}$.

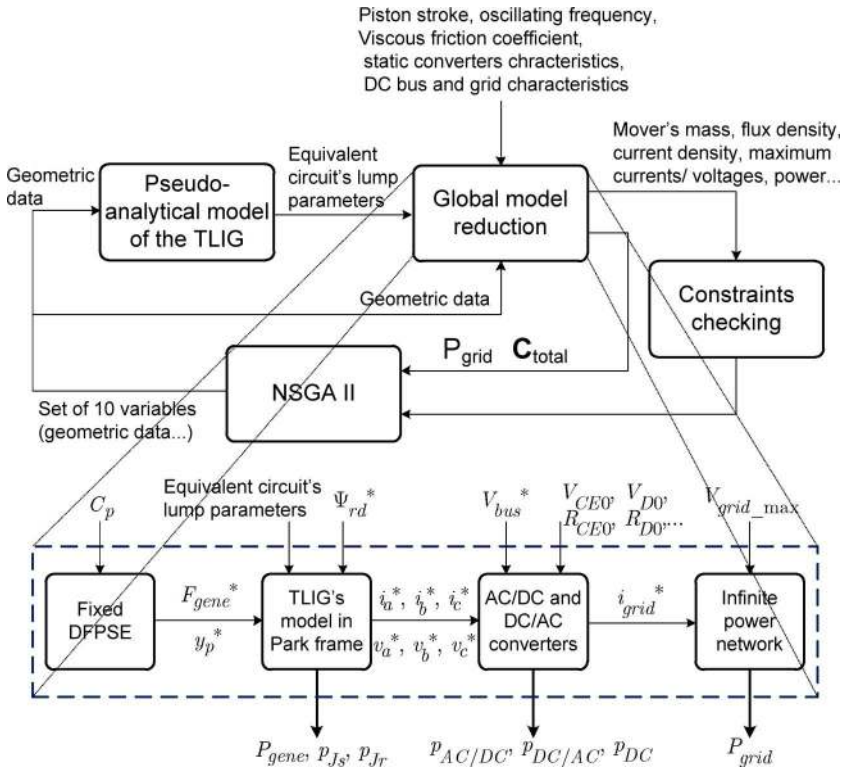

Fig. 10. Optimization process block diagram and synoptic of the reduced model.

TABLE VIII
PROBLEM FIXED DATA

Inner radii of stator winding [mm]		10
Maximum radius of the generator [mm]	$r_{\max}$	250
Maximum length of the TLIG [mm]	$L_{\max}$	1000
Maximum mover's mass [kg]	$m_{mov\ \max}$	10
Maximum current density [A/m^2]	$J_{\max}$	10
Maximum flux density in iron core [T]	$B_{\max}$	1.6
Iron cost [€/kg]	$\mathbf{C}_{Fe}$	3
Aluminum cost [€/kg]	$\mathbf{C}_{Al}$	6
Copper cost [€/kg]	$\mathbf{C}_{Cu}$	1.2

3) Multi-Constraint: First, since our system is intended for home application, the latter imposes the maximum radius and the maximum length of the generator

$$r_1 + 2e + E_{\text{mov}} + E_c \leq r_{\max} \tag{48}$$

$$L_{\text{mov}} = L_{\text{stat}} + 4.y_{p\_\max} \leq L_{\max}. \tag{49}$$

Next, the stability of the DFPSE imposes limits on the mover's mass

$$\rho_{\text{Al}} \cdot V_{\text{mov}} \leq m_{\text{mov\_ max}}. \tag{50}$$

After, the current distribution may be considered as uniform, the current density in the inductor is limited to its maximum permissible value to avoid overheating

$$J = \frac{n_t \max(I_s)}{l_e H_{st} k_{\text{coil}}} \leq J_{\max}. \tag{51}$$

Then, to maintain the validity of the pseudoanalytic electromagnetic model of the TLIG, the constraints on the maximum flux density in iron core are necessary to avoid saturation of the magnetic circuit, e.g., for the inner stator

$$B_{\text{corein}} = \frac{\max(\Psi_s)}{2p\pi n_t \left[(r_1 - H_{sl})^2 - r_0^2\right]} \leq B_{\max}. \tag{52}$$

The static converter's rated currents must also satisfy

$$\max(|i_a|, |i_b|, |i_c|) \leq i_{\text{rated\_ AC/DC}} \tag{53}$$

$$\max(|i_{\text{grid}}|) \leq i_{\text{rated\_ DC/AC}}. \tag{54}$$

Additionally, for the stability of the vector control, a constraint on the generated voltage is presented to the limit the duty cycle between [0, 1]

$$\max\left(|v_a|, |v_b, |v_c|\right) \leq \frac{V_{\text{bus}}}{2}. \tag{55}$$

Finally, a constraint for the power sent to the network is also introduced

$$F_{\text{Obj1}} \geq 0. \tag{56}$$

4) Optimization Process: The optimization process can be summarized in the diagram, Fig. 10. The optimization process implements the pseudoanalytic model of the TLIG and the

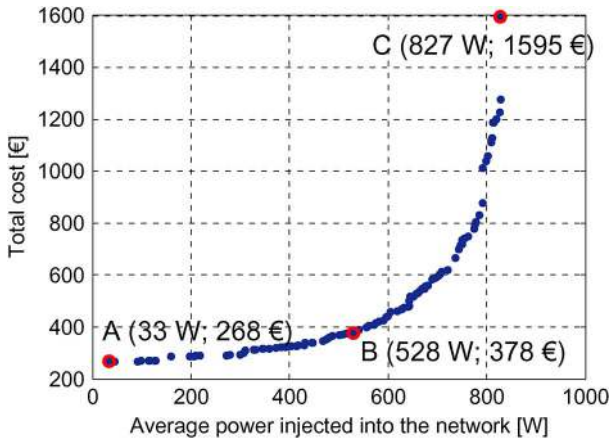

Fig. 11. Performance-cost optimization results for grid-connected TLIG.

reduced model the entire system. The optimization of the TLIG focuses on one optimal operating point of the Stirling engine (see Table V). The genetic algorithm NSGA-II is used [18]. Fixed data of the optimization study are specified in Table VIII.

C. Optimization Results and Discussion

1) Pareto Frontal: The Pareto frontal presents 100 optimal solutions which result after the calculation of 200 generations. Each solution contains an optimal TLIG with its power converters.

In Fig. 11, solution A offers the lowest overall electrical efficiency, and the least expensive investment cost. Likewise, solution C provides the highest overall performance and as expected, is the most expensive. The "middle" solution, B, provides the lowest $(f_{\mathrm{Obj2}}/f_{\mathrm{Obj1}})$ ratio [€/W].

Other optimal parameters of solution A, B, and C are detailed in Table IX. The maximum TLIG's mechanoelectrical performance (without iron-losses) that was obtained is 69.2%, whereas the maximum overall electrical efficiency of the grid-connected TLIG is 65.6%.

Semi-conductor losses are on the order of 4% of the mechanical power. If the iron losses were included, the performance could be reduced. Obviously, it depends on the quality of the magnetic material. However, as we have mentioned in the introduction, the heat due to the Joule losses and the iron losses may be harvested for the heat uses. In this case, only semiconductor losses are wasted. In addition, compared with its electrical needs, the need for heat in a home where the weather is temperate or cold, is more important.

From geometric data inTable IX, the structure of the three typical TLIGs A, B, and C can be drawn in Fig. 12.

2) Theoretical Verification of the Model Reduction: Parameters of optimal TLIGs (see Table IX) have been introduced into the complete simulation (see Section II-C) in order to verify the optimization results obtained by using the reduced model.

The complete simulation, respectively gives 2.7%, 42.1%, and 66.0% as the overall electrical efficiency of grid-connected TLIGs corresponding to solutions A, B, and C. Hence, the results on the overall electrical efficiency given by the reduced model (see Table IX) are very close to the results of the

TABLE IX
PARAMETERS OF SOME TYPICAL OPTIMAL MACHINES

	Machine A	Machine B	Machine C
r_0 [mm]	23.3	28.4	41.3
H_{sl} [mm]	22.1	27.5	36.0
E_{mov} [mm]	1.2	1.7	4.6
$l_e = l_t = \tau/6$ [mm]	10.7	14.9	36.9
p	2	2	2
E_c [mm]	5.3	5.8	35.5
n_t	147	149	176
I_{sd} [A]	9.1	11.3	11.3
$i_{rated\ \ AC/DC}$ [A]	13	14	99
$i_{rated\ \ DC/AC}$ [A]	1	4	19
$S_{AC/DC}$ [VA]	5200	5600	39600
$S_{DC/AC}$ [VA]	400	1600	7600
C_{bus} [µF]	799	1931	2460
R_s [Ω]	1.4	1.0	0.6
R_r' [Ω]	18.7	13.0	6.2
$L_m = M$ [mH]	119.8	165.5	374.3
l_{fs} [mH]	18.7	21.2	21.8
l_{fr}' [mH]	13.5	15.4	8.7
Total mass [kg]	16.7	35.2	295.8
Maximum force/moving mass ratio [N/kg]	2054	869	105
Total Joule losses [W]	1183	669.2	388.0
TLIG's mechano-electrical performance [%]	**6.1**	**46.8**	**69.2**
Total semiconductor losses [W]	40.4	59.6	41.6
Overall electric efficiency [%]	**2.6**	**41.9**	**65.6**

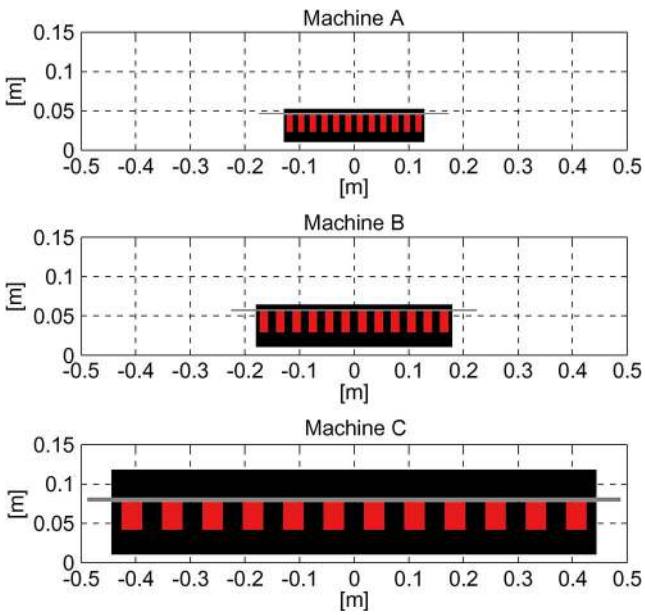

Fig. 12. Longitudinal half-section of three typical optimal machines.

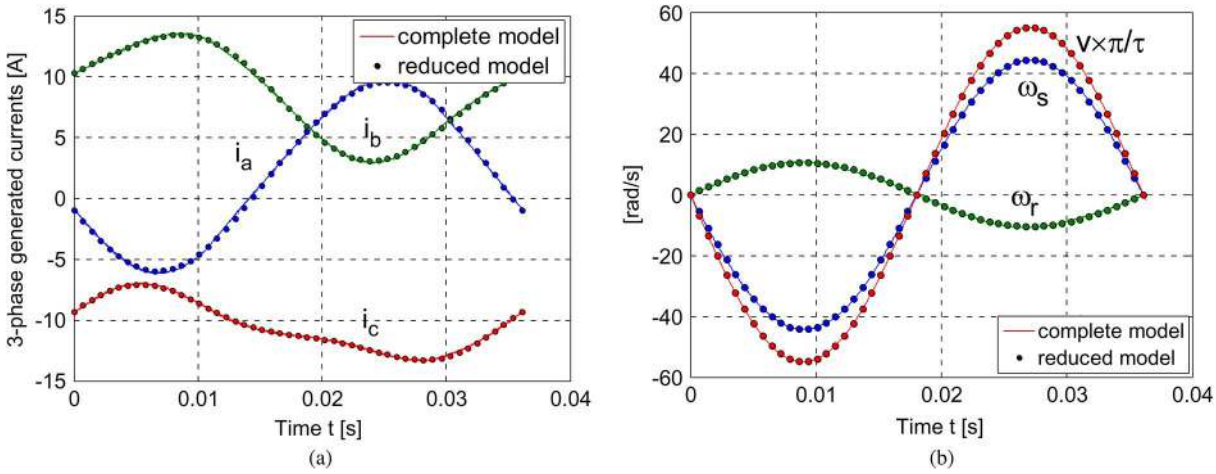

Fig. 13. Comparison between the complete simulation's results and the reduced model's results (used in optimization process) for machine C. (a) Three-phase generated currents of the TLIG and (b) angular frequencies.

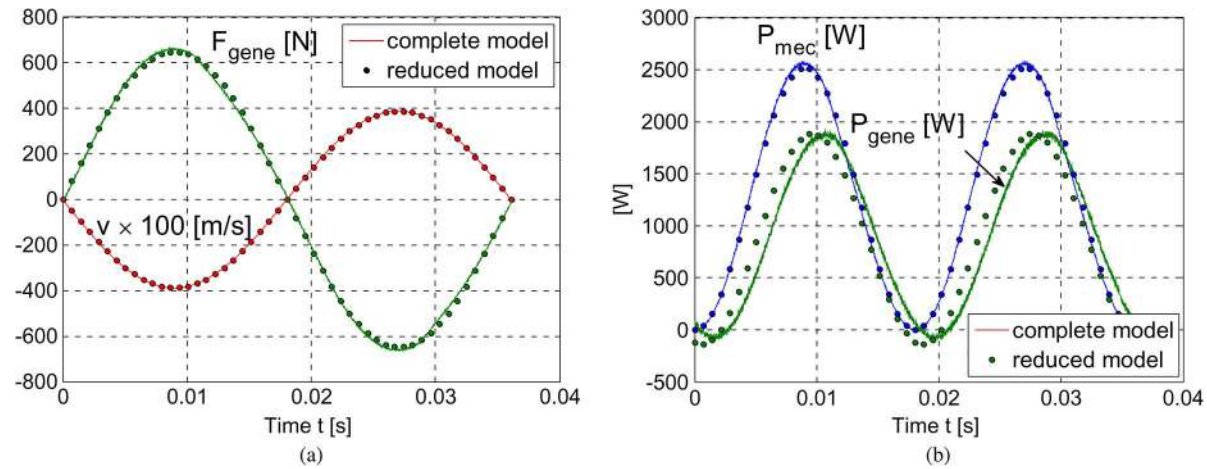

Fig. 14. Comparison between the complete simulation's results and the reduced model's results (used in optimization process) for machine C. (a) Force and piston/mover's velocity and (b) instantaneous mechanical and electrical power.

complete simulation. Therefore, the effectiveness of the model reduction is proved.

The good correlation between the two models is also obtained concerning three-phase generated currents, force, velocity, mechanical and electrical power waveforms. In Figs. 13 and 14, the results of the complete simulation which uses the parameters of the machine C (see Table IX) are presented are presented by continuous lines, whereas those of the "reduced model" by points.

Indeed, the complete simulation was performed with Euler solver with the integration step of 10^{-5} second, whereas the model reduction calculate 50 values within a mechanical cycle of the piston and without control loops. As shown in Fig. 13. a, the waveform of the generated currents is not sinusoidal, containing the mechanical harmonic $(2\pi f_{\rm osc})$ and electrical harmonic (ω_s), which is a variable in time [Fig. 13(b)]. In Fig. 14(a), the TLIG's resisting force is in opposite phase with the piston's velocity, this means that the TLIG reacts like a damper toward the DFPSE. The instantaneous generated electric power is delayed with respect to the mechanical power. Almost electric power is generated when the piston/mover decelerates [Fig. 14(b)].

This comparison thus shows the effectiveness of the "reduced model" of reducing significantly the optimization process's runtime.

3) Influences of the Stirling Engine's Operating Point on the Performance of the TLIG:

a) Influences of the oscillating frequency: As already mentioned, the feasible resonant oscillating frequency $(f_{\rm osc})$ of the DFPSE is between 20 and 35 Hz [5].

By varying the oscillating frequency from 20 to 34 Hz by a step of 2 Hz, we keep the average mechanical power constant at 1260 W. The results (see Fig. 15, Table X, and Fig. 16) demonstrate that the TLIG's efficiency is clearly better with high oscillating frequencies than with low frequencies. From 20 Hz to 30 Hz, the TLIG's performance progressively increases. However, above 30 Hz, the TLIG's performance cannot rise any further.

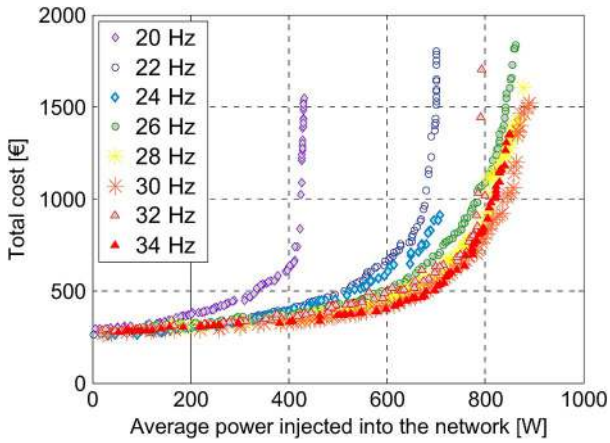

Fig. 15. Optimization results for different oscillating frequencies while maintaining constant the mechanical power (1260 W).

TABLE X
OPERATING POINTS WITH VARIABLE OSCILLATING FREQUENCY

f_{osc} [Hz]	$\max\left(\dot{y}_p\right)$ [m/s]	$\max\left(\ddot{y}_p\right)$ [m/s²]	$\max\left(F_{gene}\right)$ [N]	$\max\left(P_{grid}\right)$ [W]
20	2.8	352	898	432
22	3.1	426	816	701
24	3.4	507	748	707
26	3.6	595	691	862
28	3.9	690	641	878
30	**4.2**	**792**	**599**	**891**
32	4.5	901	561	792
34	4.8	1018	528	849

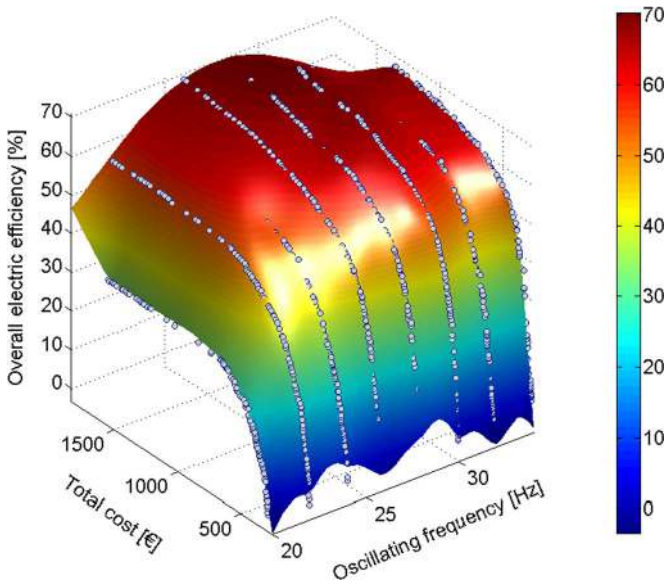

Fig. 16. Three-dimensional representation of optimization results for different oscillating frequencies when the mechanical power is kept to be constant.

The following Table X summarizes the dynamics of the piston/mover and the TLIG's maximum efficiency for different oscillating frequencies, based on the optimization results with reduced model. The best performance is obtained at $f_{\text{osc}} = 30$ Hz. Therefore, for the design phase of the DFPSE, the

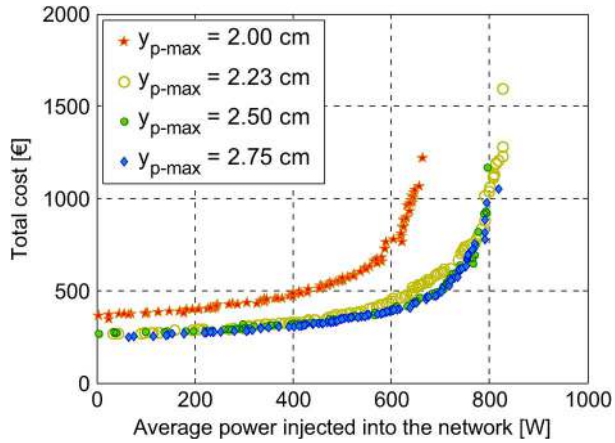

Fig. 17. Optimization results for different piston/mover's stroke when the mechanical power is maintained constant.

TABLE XI
OPERATING POINTS WITH VARIABLE PISTON'S STROKE

$y_{p\_\max}$ [cm]	$\max\left(\ddot{y}_p\right)$ [m/s²]	$\max\left(F_{gene}\right)$ [N]	$\max\left(P_{grid}\right)$ [W]	Total cost [€]
2.0	605	720	665	1219
2.23	**676**	**646**	**827**	**1595**
2.5	757	573	796	1169
2.75	833	525	818	1052

recommended operating point of the DFPSE which allows for maximization of the TLIG's performance is around 30 Hz.

These results show also that in order to reach the overall electric efficiency of the grid-connected TLIG of 65% (or more), the resonant oscillating frequency must be higher than 26 Hz, i.e., an acceleration more than 600 m/s². Otherwise, above 26 Hz, the TLIG achieves more important performance levels at less cost.

b) Influence of the Piston's stroke: Similarly, the performance of the TLIG under the influence of the piston's stroke is considered. The mechanical power is also maintained constant at 1260 W.

Based on the optimization results for different piston's stroke (see Fig. 17), the amplitude of the piston/mover's stroke proposed in this study (2.23 cm) is a however good value for maximizing the generator's performance. We cannot reduce this value, for example, to 2.0 cm at the risk of significantly diminish the overall electric efficiency (see Fig. 17).

However, if technically possible, an extension the piston's stroke to 5 cm or even to 5.5 cm can bring about a higher performance and a lower cost (see Table XI and Fig. 17).

IV. CONCLUSION

Taking into account the advantages of the TLIG (such as natural levitation, no springs, no wears, low friction, low cost,...), and its possible use in Stirling microcogenerator system, this paper has presented the sizing optimization of the TLIG applied in an original high acceleration dual free-piston Stirling microcogenerator system.

The main contribution was first to demonstrate that, with the optimization approach, the performance of the TLIG can be very appreciable for this application. The overall electric efficiency of the grid-connected TLIG can achieve up to 70%. Aside from the iron losses, the calculation has taken into account all Joule losses, semiconductor losses and DC bus capacitor losses. The optimization results also indicate that the higher is the oscillating frequency (up to 35 Hz), and the longer is the piston's travel (up to 5.5 cm), the more efficient the TLIG can be.

The particularity in this application is that the TLIG is completely submerged in the working gas of the Stirling engine's cool space. Due to this fact, the generator can be continuously cooled, and thus, all Joule losses and iron losses do not constitute "true losses" for the entire system but can be harvested for the use of heat.

After, the study has concerned also the economic aspect. In this model, with technically valid cost of raw material, all optimal solutions present a total investment cost (TLIG + power converters) limited between 0 and 1600 €.

Furthermore, this paper has presented the complete process of modeling, simulation, and optimization for electric devices based on TLIG applied in a free-piston Stirling μ-CHP system. The model reduction of the system which effectively substitute the complete simulation was a good stage to reduce significantly the runtime of the optimization process.

The experimental tests performed on the prototype helped to ensure the validation of the pseudoanalytical model using the cylindrical current sheet method, and to validate the effectiveness of the vector control.

APPENDIX

All the variables and constants in the Appendix are specified in Fig. 3 and/or Table III.

Carter Coefficient: This coefficient is calculated by an empirical formula presented in [1]

$$K_C = \frac{5\left(2e + E_{\text{mov}}\right)/\tau + l_e/\tau}{5\left(2e + E_{\text{mov}}\right)/\tau + l_e/\tau - m\left(l_e/\tau\right)^2}. \tag{A.1}$$

Fourier Series Development of the Stator Current: For our TLIG structure, the expression of the stator current taking into account the slots and ends effect is

$$J_{s\theta} = \sum_{\zeta=1,3,5,7\ldots} \sum_{p=1,5,7,11,\ldots} \frac{12 J_{sm}}{\pi^2 \zeta p} \sin\left(\frac{p\pi}{12}\right) \sin\left(\frac{\zeta L_{\text{stat}} \pi}{L}\right) \ldots \left\{ e^{j\left[\frac{\pi}{\tau}\left(p+\frac{2\tau\zeta}{L}\right) z \pm \omega_s t\right]} + e^{j\left[\frac{\pi}{\tau}\left(p-\frac{2\tau\zeta}{L}\right) z \pm \omega_s t\right]} \right\}. \tag{A.2}$$

- J_{sm} is the magnitude of the line-current intensity [A/m] [see (5)],
- L is the "modulation length," Fig. 18,
- the sign $\ll - \gg$ is assigned, whereas $p = 1, 7, 13, \ldots, 3q+1$; and the sign $\ll + \gg$, whereas $p = 5, 11, \ldots, 3q-1$ with q, a integer.

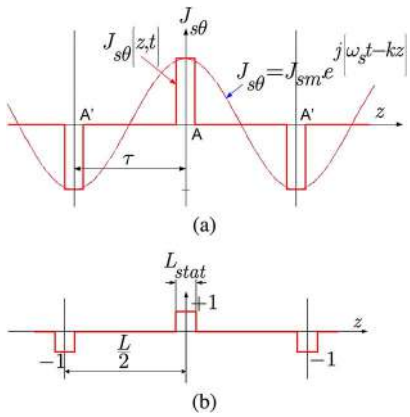

Fig. 18. Distributions of the stator current along the z-axis that take into account (a) slots effect and (b) ends effect.

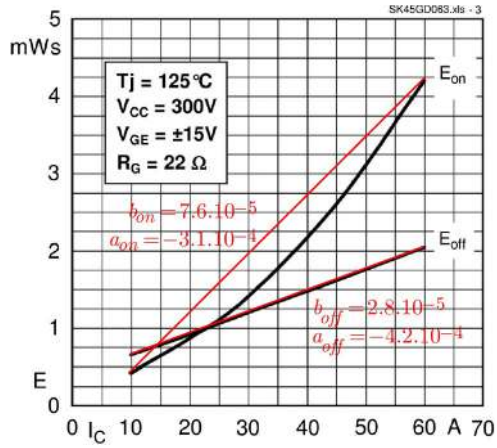

Fig. 19. Switching losses as a function of current in case of a 50-A rated current converter.

Stator Inductance Leakage Calculation:

$$l_{fs} \propto \frac{4\pi\mu_0 p n_t^2}{l_e H_{sl}^2} \left[\frac{1}{4}\left(r_1^4 - r_0^4\right) - \frac{2}{3} r_0 \left(r_1^3 - r_0^3\right) + \frac{1}{2} r_0^2 \left(r_1^2 - r_0^2\right)\right]. \tag{A.3}$$

Empirical Parameters of Static Converters' Losses Model: For the simplicity of the model, switching losses are considered as linear functions of the rated current

$$E_{\text{on}} = b_{\text{on}} \cdot i_{\text{rated}} + a_{\text{on}}$$

$$E_{\text{off}} = b_{\text{off}} \cdot i_{\text{rated}} + a_{\text{off}}$$

hence E_{on}, E_{off} [J] are the turn-on and turn-off losses of each IGBT.

In the optimization process, empirical formulas of the coefficients a_{on}, a_{off}, b_{on}, b_{off}, according to the rated current, can be obtained from the datasheet of several Semikron's products available on the market in 2012.

a_{on}, a_{off}, b_{on}, b_{off} can then be determined for every converter (one example is shown in Fig. 19). Then, approximate

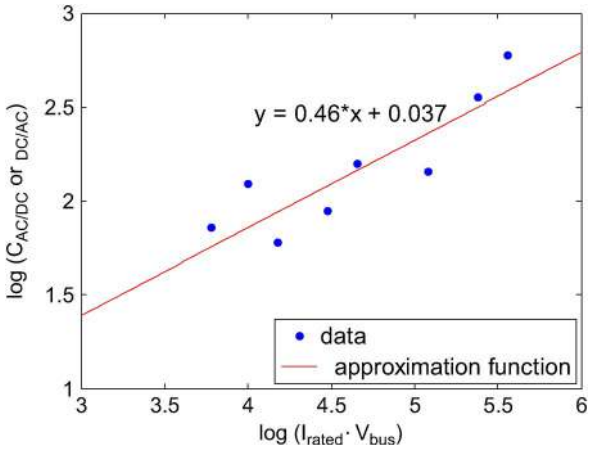

Fig. 20. Costs as a function of apparent power for each half-bridge (see Table XII).

TABLE XII
COST OF POWEREX'S HALF-BRIDGES

Apparent power [kVA]	Cost [€]
6	72,3
10	123,6
15	60,6
30	89,0
45	158,0
120	144,0
240	357,0
360	600,0

continuous functions of these parameters according to the rated current are given by

$$\begin{aligned} a_{\text{on\_AC/DC}} &= -10^{-6}\left(i_{\text{rated\_AC/DC}}\right)^2 \\ &\quad + 2.10^{-5} i_{\text{rated\_AC/DC}} - 1.6.10^{-3} \\ b_{\text{on\_AC/DC}} &= 3.10^{-8}\left(i_{\text{rated\_AC/DC}}\right)^2 \\ &\quad + 2.10^{-6} i_{\text{rated\_AC/DC}} + 2.10^{-4} \\ a_{\text{off\_AC/DC}} &= 2.10^{-5} i_{\text{rated\_AC/DC}} + 6.10^{-5} \\ b_{\text{off\_AC/DC}} &= 5.10^{-7} i_{\text{rated\_AC/DC}} + 3.10^{-5}. \end{aligned}$$

We can also obtain from Semikron's datasheet

$$\begin{aligned} V_{\text{CE0\_AC/DC}} &= 1.1 \\ R_{\text{CE0\_AC/DC}} &= 1.119 i_{\text{rated\_AC/DC}}^{-0.993} \\ V_{D0\text{\_AC/DC}} &= 2.10^{-5}\left(i_{\text{rated\_AC/DC}}\right)^2 \\ &\quad - 24.10^{-4} i_{\text{rated\_AC/DC}} + 0.958 \\ R_{D0\text{\_AC/DC}} &= 0.3826\left(i_{\text{rated\_AC/DC}}\right)^{-0.74} \end{aligned}$$

where $V_{\text{CE0\_(AC/DC)}}$, $V_{D0\text{\_(AC/DC)}}$ [V], respectively are voltage losses across an IGBT and a diode of the three-phase converter; $R_{\text{CE0\_(AC/DC)}}$, $R_{D0\text{\_(AC/DC)}}$ [Ω], respectively are resistances of an IGBT or a diode of the three-phase converter.

Empirical Formula of Converters' Cost: The data in Fig. 20 is based on Powerex's modules.

REFERENCES

[1] D. J. de Groot and C. J. Heuvelman, "Tubular linear induction motor for use as a servo actuator," *Proc. Inst. Elect. Eng.—Electric Power Appl.*, vol. 137, no. 4, pp. 273–280, Jul. 1990.

[2] P. R. Austin and A. R. Eastham, "Helically wound linear induction pump for molten nonferrous metals," *IEEE Trans. Ind. Appl.*, vol. IA-21, no. 3, pp. 738–748, May 1985.

[3] G. Becherini, "Gyroscopic stabilization of launch package in induction type coilgun," *IEEE Trans. Magn.*, vol. 37, no. 1, pp. 116–122, Jan. 2001.

[4] T. G. Engel, J. M. Neri, and M. J. Veracka, "Solid-projectile helical electromagnetic launcher," *IEEE Trans. Plasma Sci.*, vol. 37, no. 4, pp. 603–607, Apr. 2009.

[5] J. Boucher, F. Lanzetta, and P. Nika, "Optimization of a dual free piston Stirling engine," *Appl. Thermal Eng.*, vol. 27, no. 4, pp. 802–811, Mar. 2007.

[6] Z. Zabar, X. N. Lu, L. Birenbaum, E. Levi, and J. L. He, "A 500 Rn/s linear induction launcher," in *Proc. 8th IEEE Int. Pulsed Power Conf. Dig. Tech. Papers*, 1991, pp. 58–62.

[7] I. Boldea and S. A. Nasar, "Linear electric actuators and generators," in *IEEE Int. Elect. Mach. Drives Conf. Rec.*, 1997, pp. MA1/1.1–MA1/1.5.

[8] V. Di Dio, R. Miceli, and M. Trapanese, "The use of sea waves for generation of electrical energy: A linear tubular asynchronous electrical generator," in *Proc. OCEANS*, 2007, pp. 1–4.

[9] A. Demenko *et al.*, "Optimisation of a tubular linear machine with permanent magnets for wave energy extraction," *COMPEL—Int. J. Comput. Math. Elect. Electron. Eng.*, vol. 30, pp. 1056–1068, 2011.

[10] A. Pirisi, M. Mussetta, G. Gruosso, and R. E. Zich, "An optimized three phase TPM-LiG for marine applications," in *Proc. Int. SPEEDAM*, 2010, pp. 1712–1717.

[11] N. J. Baker, M. A. Mueller, and E. Spooner, "Permanent magnet air-cored tubular linear generator for marine energy converters," in *Proc. 2nd Int. Conf. (Conf. Publ. No. 498) PEMD*, 2004, vol. 2, pp. 862–867.

[12] X. Wang, Z. Wu, L. Li, J. Deng, and Y. Luan, "Control system of linear engine for hybrid electric vehicle," *J. Autom. Safety Energy*, vol. 2, no. 4, pp. 338–344, 2011.

[13] W. R. Cawthorne *et al.*, "Development of a linear alternator-engine for hybrid electric vehicle applications," *IEEE Trans. Veh. Technol.*, vol. 48, no. 6, pp. 1797–1802, Nov. 1999.

[14] J. H. H. Alwash, A. D. Mohssen, and A. S. Abdi, "Helical motion tubular induction motor," *IEEE Trans. Energy Convers.*, vol. 18, no. 3, pp. 362–369, Sep. 2003.

[15] J. L. He, E. Levi, Z. Zabar, and L. Birenbaum, "Equivalent circuits and parameters for induction-type electromagnetic launchers," *IEEE Trans. Magn.*, vol. 29, no. 1, pp. 667–674, Jan. 1993.

[16] A. Musolino, R. Rizzo, and E. Tripodi, "The double-sided tubular linear induction motor and its possible use in the electromagnetic aircraft launch system," *IEEE Trans. Plasma Sci.*, vol. 41, no. 5, pp. 1193–1200, May 2013.

[17] J. Fleszar and E. A. Mendrela, "Twin-armature rotary-linear induction motor," *Proc. Inst. Elect. Eng.—Elect. Power Appl.*, vol. 130, no. 3, pp. 186–192, May 1983.

[18] K. Deb, A. Pratap, S. Agarwal, and T. Meyarivan, "A fast and elitist multiobjective genetic algorithm: NSGA-II," *IEEE Trans. Evol. Comput.*, vol. 6, no. 2, pp. 182–197, Apr. 2002.